



Deep HI Mapping of Stephan’s Quintet and Its Neighborhood

Cheng Cheng^{1,2,3}, Cong Kevin Xu^{1,2}, P. N. Appleton⁴, P.-A. Duc⁵, N.-Y. Tang⁶, Y.-S. Dai¹, J.-S. Huang^{1,7},
U. Lisenfeld^{8,9}, F. Renaud¹⁰, Chuan He¹, and Hai-Cheng Feng^{11,12,13}

¹ Chinese Academy of Sciences South America Center for Astronomy, National Astronomical Observatories, CAS, Beijing 100101, People’s Republic of China
xucong@nao.cas.cn

² National Astronomical Observatories, Chinese Academy of Sciences, 20A Datun Road, Chaoyang District, Beijing 100101, People’s Republic Of China

³ CAS Key Laboratory of Optical Astronomy, National Astronomical Observatories, Chinese Academy of Sciences, Beijing 100101, People’s Republic of China

⁴ Caltech/IPAC, MC 6-313, 1200 E. California Boulevard, Pasadena, CA 91125, USA

⁵ Université de Strasbourg, CNRS, Observatoire astronomique de Strasbourg, UMR 7550, F-67000 Strasbourg, France

⁶ Department of Astronomy, University of Massachusetts, Amherst, MA 01003, USA

⁷ Center for Astrophysics | Harvard & Smithsonian, 60 Garden Street, Cambridge, MA 02138 USA

⁸ Dept. Física Teórica y del Cosmos, Campus de Fuentenueva, Edificio Mecenas, Universidad de Granada, E-18071 Granada, Spain

⁹ Instituto Carlos I de Física Teórica y Computacional, Facultad de Ciencias, E-18071 Granada, Spain

¹⁰ Department of Astronomy and Theoretical Physics, Lund Observatory, Box 43, SE-221 00 Lund, Sweden

¹¹ Yunnan Observatories, Chinese Academy of Sciences, Kunming 650011, Yunnan, People’s Republic of China

¹² University of Chinese Academy of Sciences, Beijing 100049, People’s Republic of China

¹³ Key Laboratory for the Structure and Evolution of Celestial Objects, Chinese Academy of Sciences, Kunming 650011, Yunnan, People’s Republic of China

Received 2023 March 28; revised 2023 June 1; accepted 2023 June 17; published 2023 August 23

Abstract

We carried out deep mapping observations of the atomic hydrogen (HI) 21 cm line emission in a field centered on the famous galaxy group Stephan’s Quintet (SQ), using the Five-hundred-meter Aperture Spherical Telescope (FAST) equipped with a 19-beam receiver. The final data cube reaches an HI column density sensitivity of $5\sigma = 2.1 \times 10^{17} \text{ cm}^{-2}$ per 20 km s^{-1} channel with an angular resolution of $4''.0$. The discovery of a large diffuse feature of the HI emission in the outskirts of the intragroup medium of SQ was reported in a previous paper (Xu et al.). Here we present a new study of the total HI emission of SQ and the detection of several neighboring galaxies, exploiting the high sensitivity and the large sky coverage of the FAST observations. A total HI mass of $M_{\text{HI}} = 3.48 \pm 0.35 \times 10^{10} M_{\odot}$ is found for SQ, which is significantly higher than previous measurements in the literature. This indicates that, contrary to earlier claims, SQ is not HI deficient. The excessive HI gas is mainly found in the velocity ranges of $6200\text{--}6400 \text{ km s}^{-1}$ and $6800\text{--}7000 \text{ km s}^{-1}$, which were undetected in previous observations that are less sensitive than ours. Our results suggest that the “missing HI” in compact groups may be hidden in the low-density diffuse neutral gas instead of in the ionized gas.

Unified Astronomy Thesaurus concepts: [Hickson compact group \(729\)](#); [Galaxy groups \(597\)](#); [HI line emission \(690\)](#)

1. Introduction

Galaxies are formed in hierarchical structures in the Universe. Galaxy–galaxy interaction plays an important role in the formation and evolution of galaxies. Compact groups, characterized by aggregates of four to eight galaxies with spatial densities as high as those in cluster cores (Hickson 1982), represent a special class of interacting systems completely different from merging pairs that trigger the most extreme starbursts (star formation rate (SFR) $> 100 M_{\odot} \text{ yr}^{-1}$) in the local Universe (Sanders 1996). Galaxies in compact groups show very diversified SFRs, but none with a detected SFR $> 100 M_{\odot} \text{ yr}^{-1}$ (Lenkić et al. 2016). Their SFRs depend sensitively on the HI abundance, which is generally deficient (Verdes-Montenegro et al. 2001; Johnson et al. 2007). Discovered as an aggregation of nebulae in 1877 (Stephan 1877), Stephan’s Quintet (SQ) is arguably the best-studied compact group. It has been observed in nearly all accessible wave bands from X-rays, UV, visible, to IR and radio (Allen & Hartsuiker 1972; van der Hulst & Rots 1981; Shostak et al. 1984; Moles et al. 1997; Yun et al. 1997;

Xu et al. 1999; Gao & Xu 2000; Gallagher et al. 2001; Sulentic et al. 2001; Williams et al. 2002; Xu et al. 2003; Lisenfeld et al. 2004; Trinchieri et al. 2005; Xu et al. 2005; Appleton et al. 2006), and high-resolution observations of SQ’s IR emission were included in the James Webb Space Telescope’s first public release (Pontoppidan et al. 2022). It has been found that the HI gas is all in the intragroup medium outside the member galaxies in SQ (Shostak et al. 1984; Williams et al. 2002), and its spiral members show unenhanced SFRs (Xu et al. 2005). Most strikingly, Allen & Hartsuiker (1972) discovered in the intragroup medium of SQ a very large shock front of $\sim 40 \text{ kpc}$ in size which, among all known intergalactic shock fronts, is second only to that of the radio relics caused by cluster mergers (Enßlin 2002). This shock was triggered by a high-velocity ($\sim 1000 \text{ km s}^{-1}$) intruder (NGC 7318b) currently colliding into a debris field in the intragroup medium, the latter being a product of previous interactions among other member galaxies of the group (Allen & Hartsuiker 1972; van der Hulst & Rots 1981; Moles et al. 1997; Sulentic et al. 2001). SQ has provided an excellent laboratory for studies of various processes associated with high-speed galaxy collisions, such as the heating and cooling of warm H_2 gas powered by large-scale shocks (Appleton et al. 2017; Guillard et al. 2022), SFR quenching by turbulence in postshock molecular gas (Guillard & Boulanger 2012), and the formation of Green Valley



Original content from this work may be used under the terms of the [Creative Commons Attribution 4.0 licence](#). Any further distribution of this work must maintain attribution to the author(s) and the title of the work, journal citation and DOI.

galaxies in galaxy groups (Cluver et al. 2013; Alatalo et al. 2014; Lisenfeld et al. 2017). These studies provide important constraints to galaxy formation/evolution models, in particular for the high- z Universe when galaxies have very low metallicity and may collide with each other more frequently.

A comprehensive understanding of the properties of SQ depends crucially on how accurately we know its interaction history, which is very complex due to the relatively large number of participants ($N \geq 5$). Theoretical simulations have yielded inconclusive and controversial results. The fiducial model in Renaud et al. (2010) involves a number of events in the last half billion years, including collisions between the spiral galaxies NGC 7319 and NGC 7320c, creating the so-called outer tail, between NGC 7319 and the early-type galaxy NGC 7318a, creating the inner tail, and between the high-speed intruder NGC 7318b and the intragroup medium, producing shocks in the gas stripped by the previous interactions. However, the hydrodynamical simulations in Hwang et al. (2012) favor a different scenario in which both the outer tail and inner tail were triggered simultaneously by a close encounter between NGC 7320c and NGC 7319 about 9×10^8 years ago. It provides a better fit to the current positions of galaxies and tidal tails, though it cannot explain the observed age difference between star formation regions and star clusters in the outer and inner tails (Xu et al. 2005; Fedotov et al. 2011). It predicts that most gas is still inside galaxies, which contradicts with observations (Shostak et al. 1984; Williams et al. 2002). In both models, the role played by NGC 7317, an early-type galaxy, is neglected because of a lack of observed connection to any other SQ members. Recently a reddish, low surface brightness stellar halo surrounding SQ was discovered in deep optical imaging observations (Duc et al. 2018), which corresponds spatially very well to the diffuse X-ray halo (Trinchieri et al. 2005), in particular around NGC 7317. Its size and morphology are consistent with the formation of the galaxy group more than a billion years ago.

In order to constrain better the early history of SQ and explore the diffuse HI gas in and around the group, we carried out deep mapping observations of the diffuse HI emission in a region of $\sim 30' \times 30'$ centered on SQ using the Five-hundred-meter Aperture Spherical Telescope (FAST) equipped with a 19-beam receiver (Jiang et al. 2019, 2020; Qian et al. 2020). The HI is the least bound component of galaxies, so will be the easiest (and hence first) to be stripped off and spread around during interactions. Thus, the distribution of the diffuse HI and its velocity field can put new and crucial constraints to the interaction history models. The discovery of a large diffuse feature of the HI emission in the outskirts of intragroup medium of SQ was reported in a previous paper (Xu et al. 2022). In this paper we present other results from the same observations, with the focus on the contribution of the diffuse gas to the total HI mass in the central region of the intragroup medium, and the detection of several neighboring galaxies.

The paper is organized as follows: after this introduction, Section 2 describes the observations and the data reduction procedure. Sections 3 and 4 present our results on the HI properties of SQ and of the neighboring galaxies, respectively. Section 5 is devoted to a discussion. Finally, a summary is given in Section 6. A comoving distance of 85 Mpc for SQ is adopted from the NASA/IPAC Extragalactic Database (NED).¹⁴ For

neighboring galaxies in the field of view of the FAST observations, a Hubble constant of $H_0 = 70 \text{ km s}^{-1} \text{ Mpc}^{-1}$ is assumed.

2. Observations and Data Reduction

The FAST observations and the data reduction, including the sidelobe correction, are presented in detail in Xu et al. (2022). Here we give only a brief recount.

Observations: the observations were carried out using the FAST 19-beam receiver in the standard ON-OFF mode with a total observation time of 22.4 hr (including overheads). They consist of 16 pointings in a rectangular 4×4 grid and cover uniformly a region of $\sim 30'$ in size with 304 sky pixels (beam positions in the sky). The angular resolution is $2''.9$ and the separation between the nearest pixels is $1''.4$ in the R.A. direction and $1''.2$ in the decl. direction, therefore the mapping satisfies the Nyquist sampling criterion. The observations have a central frequency of 1391.64 MHz and a frequency coverage of 1050–1450 MHz with a frequency resolution of 7.63 kHz ($\Delta\nu = 1.65 \text{ km s}^{-1}$).

Data reduction: the spectral data of individual beams were reduced following a similar procedure as presented in Cheng et al. (2020). This includes averaging of individual samplings, calibration (converting the digital counts to flux density in mJy beam⁻¹), ON-minus-OFF, standing-waves and baseline removal, and rebinning. In addition, the sidelobes are corrected utilizing the images of individual beams (Jiang et al. 2020), which provide information on the point-spread functions (PSFs) of the beams. The end product is a data cube containing 304 spectra covering the velocity range of 4600–7600 km s⁻¹ in $\Delta\nu = 20 \text{ km s}^{-1}$ channels with a 1σ noise of 0.16 mJy beam⁻¹. The corresponding HI column density sensitivity is $1\sigma = 1.2 \times 10^{17} \text{ cm}^{-2}$ per channel. The velocity system is in the optical redshift convention and the local standard of rest (LSR) reference frame. The calibration uncertainty of FAST data is 10% (Jiang et al. 2020).

Smoothing: the data cube obtained above is highly redundant in the sense that a sky area of the size of a single beam ($D = 2''.9$) is covered by multiple beams (beam separation = $1''.4 \times 1''.2$). In order to take advantage of the redundancy and improve the sensitivity for the diffuse emission, a Gaussian kernel of FWHM = $2''.8$ is applied to the data cube. This improves the HI column density sensitivity to $1\sigma = 4.2 \times 10^{16} \text{ cm}^{-2}$ per channel with a slightly degraded angular resolution of $4''.0$.

The channel maps of the FAST observations are presented in Appendix A.

3. HI Emission of SQ

Figure 1 shows a contour map of the integrated HI emission between 5600 and 7000 km s⁻¹ overlaid on a CFHT MegaCam r -band image. The large red circle in the center, which has a diameter of $12''$ (300 kpc in linear scale), represents the aperture within which we measure the SQ's HI spectrum. In Figure 2, the spectrum is compared with those obtained previously by mapping observations using the 305 m Arecibo telescope (Peterson & Shostak 1980) and the Green Bank Telescope (GBT; Borthakur et al. 2015). Thanks to its high sensitivity, the FAST spectrum is much less noisy than the previous two results. From the FAST spectrum, the integrated HI flux of SQ is $20.5 \pm 2.1 \text{ Jy km s}^{-1}$. This is 1.2 times higher than the result of the Arecibo observations ($16.7 \pm 1.6 \text{ Jy km s}^{-1}$) and 1.7 times higher than that of the GBT ($11.8 \text{ Jy km s}^{-1}$). The HI mass can be estimated using the formula

¹⁴ NED is operated by the Jet Propulsion Laboratory, California Institute of Technology, under contract with the National Aeronautics and Space Administration.

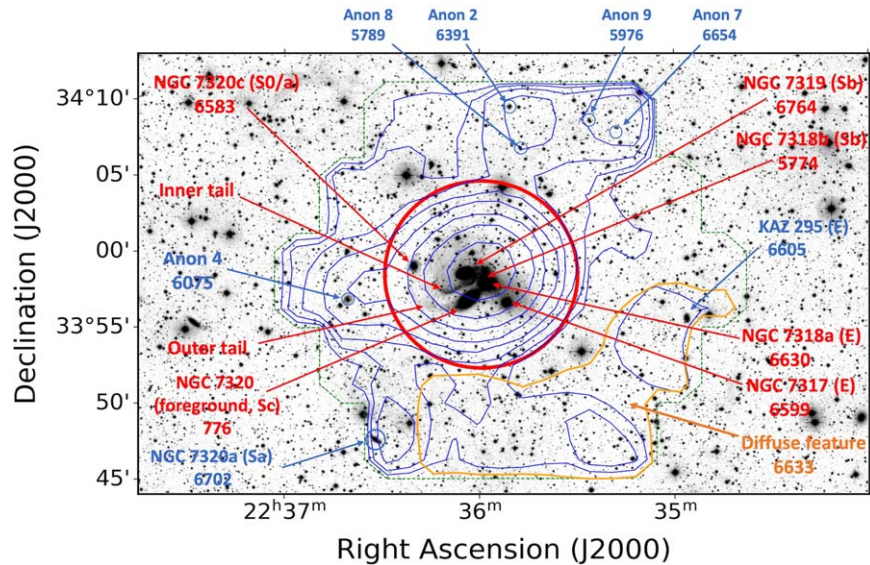


Figure 1. Contour map (in blue contours) of the integrated H I emission between 5600–7000 km s⁻¹ overlaid on an *r*-band image. The contour levels are [4, 8, 16, 32, 64, ...] × 3.5 × 10¹⁷ cm⁻². The green boundary delineates the coverage of the FAST observations. The central red circle ($D = 12'$) shows the aperture with which the total H I spectrum presented in Figure 2 is extracted. The orange line delineates the diffuse H I feature whose systemic velocity is written in brown labels (Xu et al. 2022). Provided in the figure is also information for the member galaxies and the main tidal features in SQ (in red labels), for neighboring galaxies detected by FAST (in blue labels) whose positions are marked by blue circles, and for the neighboring galaxy KAZ 295 (in blue labels). For each source, the name, Hubble type (when available), and velocity in km s⁻¹ are listed.

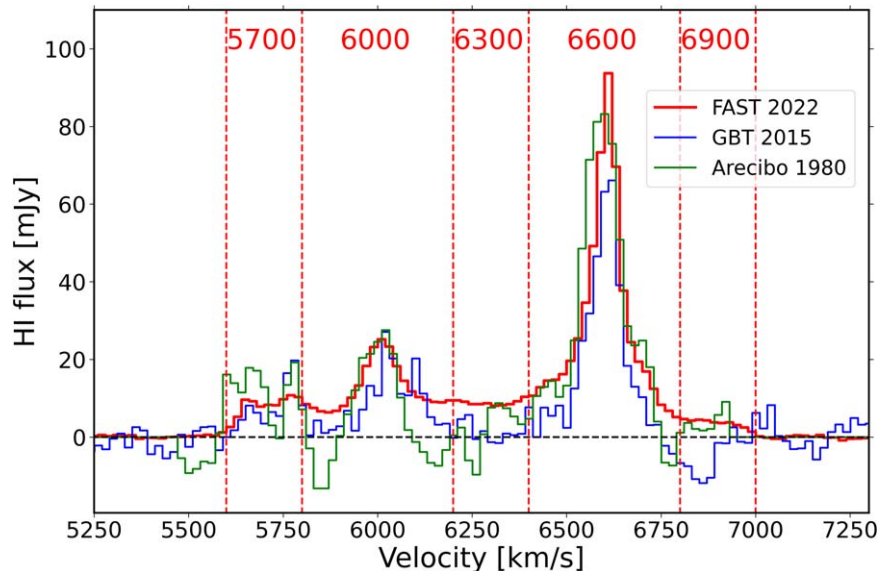


Figure 2. H I spectra of SQ obtained by FAST (red), Arecibo (green; Peterson & Shostak 1980), and GBT (blue; Borthakur et al. 2015). The red vertical dashed lines mark the boundaries of the five kinematical components. We have smoothed the Arecibo and GBT spectra to a resolution of 20 km s⁻¹ for comparison, from their original resolutions of 8.8 km s⁻¹ and 10 km s⁻¹, respectively.

$M_{\text{HI}} = 2.356 \times 10^5 D^2 S\Delta v M_{\odot}$, where D is the comoving distance in Mpc and $S\Delta v$ the integrated H I flux in Jy km s⁻¹. Accordingly, the FAST result corresponds to an H I mass of $M_{\text{HI}} = 3.48 \pm 0.35 \times 10^{10} M_{\odot}$ for SQ.

With reference to the previous high angular resolution synthetic observations of Shostak et al. (1984) and Williams et al. (2002), who resolved the H I emission in SQ into several spatially and kinematically separated features, we divide the SQ spectrum into five velocity components: 5700 component (5600–5800 km s⁻¹), 6000 component (5800–6200 km s⁻¹), 6300 component (6200–6400 km s⁻¹), 6600 component (6400–6800 km s⁻¹), and 6900 component (6800–7000 km s⁻¹). Note that these components do not include the emission

outside the velocity range of 5600–7000 km s⁻¹ whose contribution to the total H I flux is negligible (see Figure 2). The 5700 component corresponds to the “West A” feature in the Westerbork Synthesis Radio Telescope H I map of Shostak et al. (1984) and the “SW” feature in the Very Large Array (VLA) map of Williams et al. (2002), the 6000 component to the “West B” feature in Shostak et al. (1984) and the “NW-LV” feature in Williams et al. (2002), and the 6600 component to the “Main” feature in Shostak et al. (1984) and the combination of the “NW-HV,” “Arc-S,” and “Arc-N” features in Williams et al. (2002). The 6300 and 6900 components are undetected in the two synthetic maps. The contour maps of the integrated emission (i.e., moment-0 maps) in the velocity ranges of the five

components are presented in the five panels of Figure 3. Identified in these maps are also several neighboring galaxies of SQ which will be discussed in detail in the next section. For comparison, contours of the high-resolution VLA maps adopted from Williams et al. (2002) are plotted in the figures for the 5700, 6000, and 6600 components.

As shown in Figures 3(a) and (b), the 5700 and 6000 components are only marginally resolved by FAST. The 2D Gaussian fittings of the unsmoothed FAST maps find sizes of 3/2 and 3/1 for the two components, respectively. These respectively correspond to intrinsic sizes of 1/5 and 1/3 after the PSF deconvolution, consistent with the VLA measurements (Williams et al. 2002). According to Williams et al. (2002), the 5700 component is associated with the “new intruder” NGC 7318b whose radial velocity is 5774 km s^{-1} . Its HI mass measured by FAST is $M_{\text{HI}} = 2.43 \pm 0.24 \times 10^9 M_{\odot}$. This is consistent with the result from the Westerbork Synthesis Radio Telescope ($M_{\text{HI}} = 2.4 \pm 0.6 \times 10^9 M_{\odot}$; Shostak et al. 1984) and higher than the VLA value ($1.5 \pm 0.2 \times 10^9 M_{\odot}$; Williams et al. 2002). Peterson & Shostak (1980) found a higher HI mass for this component in their Arecibo mapping observations ($M_{\text{HI}} = 5.1 \pm 1.8 \times 10^9 M_{\odot}$), although the difference from our result is only at the 1.5σ level because of the large error.

The origin of the 6000 component is still controversial. Based on the observations of Shostak et al. (1984), Moles et al. (1997) suggested that it is also associated with NGC 7318b and the redshift difference from the 5700 component is due to the rotation of an HI disk. This was disputed by Williams et al. (2002) who argued that the VLA observations, which have better angular resolution and flux sensitivity than those of the Westerbork Synthesis Radio Telescope, demonstrate that the 5700 and the 6000 components are distinctly separated both in the spatial and in the velocity domains, so are very unlikely to be associated with the same HI disk. We find an HI mass of ($M_{\text{HI}} = 8.34 \pm 0.83 \times 10^9 M_{\odot}$) for the 6000 component. This is higher than the results in the literature, which are $5.3 \pm 1.5 \times 10^9 M_{\odot}$, $3.1 \pm 0.4 \times 10^9 M_{\odot}$ and $2.2 \pm 0.3 \times 10^9 M_{\odot}$ by Peterson & Shostak (1980), Shostak et al. (1984), and Williams et al. (2002), respectively.

Previously, the 6300 component of the HI 21 cm line emission was only marginally detected by GBT observations (Borthakur et al. 2010, 2015). On the other hand, emissions in the velocity range of 6200–6400 km s^{-1} have been detected in SQ in many other bands, including the millimeter CO rotation line emission of molecular gas (Guillard & Boulanger 2012; Yttergren et al. 2021), the far-IR [C II] and [O I] fine structure line emissions (Appleton et al. 2013, 2017), emissions of the Balmer recombination lines and other emission lines of ionized gas in the optical (Xu et al. 2003; Iglesias-Páramo et al. 2012; Duarte Puertas et al. 2019; Yttergren et al. 2021; Guillard et al. 2022), and the $\text{Ly}\alpha$ line emission in the UV (Guillard et al. 2022). All of these detections of different emission lines, with angular resolutions ranging from subarcseconds to $50''$, are consistent with shock excitation. The radiations are mainly from two locations: (1) the large shock front and (2) the so-called “bridge” that links the Seyfert 2 nucleus of NGC 7319 and the shock front (Cluver et al. 2010). Some subregions in the large shock front show emissions in the velocity range of 6200–6400 km s^{-1} in the wings of relatively broad lines ($\Delta v > 300 \text{ km s}^{-1}$), peaking near 6000 or 6600 km s^{-1} (Guillard & Boulanger 2012; Iglesias-Páramo et al. 2012; Appleton et al. 2013, 2017; Guillard et al. 2022). Guillard & Boulanger (2012) attributed these emissions to postshock gas that condensed out of

the shock-heated hot X-ray gas after cooling down. There is a major difference between the large shock front and the bridge: in the radio continuum the former is very bright but the latter is undetected (Xu et al. 2003), indicating that the shocks in the two regions are different. The fact that the bridge is spatially and kinematically linked to the 4 kpc outflow (Aoki et al. 1996) strongly suggests that the shocks in the bridge are powered by the outflow, and the radio quietness may be explained by the low efficiency of these shocks in accelerating cosmic-ray electrons. On the other hand, new JWST and Atacama Large Millimeter/submillimeter Array (ALMA) observations with subarcsecond resolutions detected in the bridge several filaments whose connection to the outflow is unclear (Appleton et al. 2023). The 2D Gaussian fitting of the 6300 component finds a size of $4/0 \times 3/4$, corresponding roughly to an intrinsic size of $2/9 \times 1/9$ after the beam deconvolution under the assumption that the emission can be approximated by a Gaussian source. Its HI mass is $M_{\text{HI}} = 2.94 \pm 0.30 \times 10^9 M_{\odot}$.

The 6600 component, containing the majority of the HI emission associated with SQ (Figure 2), shows a strong central source plus low-level emissions in the outskirts. In particular, an arm/tail-like diffuse feature on the south of SQ has been discovered within this component (Xu et al. 2022). The HI gas in the diffuse feature, which is outside the aperture within which the SQ spectrum is extracted (Figure 1), is confined in the velocity range of 6550–6750 km s^{-1} . The HI mass of the 6600 component of SQ is $M_{\text{HI}} = 1.91 \pm 0.19 \times 10^{10} M_{\odot}$, which is 56% of the total HI mass of the SQ system.

The 6900 component was not detected in previous HI observations, but appeared in the observations of the CO emission of the molecular gas (Guillard & Boulanger 2012; Guillard et al. 2022) and in the surveys of H II regions (Sulentic et al. 2001; Iglesias-Páramo et al. 2012; Duarte Puertas et al. 2019). The FAST map of the component (Figure 3(e)) centers very close to the intragroup starburst SQ-A (Xu et al. 1999), in agreement with the locations of the CO and $\text{H}\alpha$ emissions. The FAST observations do not resolve the component. The $\text{H}\alpha$ data cube of Duarte Puertas et al. (2019), which has an average angular resolution of $0''.8$, shows that this component is extended from SQ-A toward the shock front, presumably associated with preshock gas in the debris field. The HI mass of the 6900 component is $M_{\text{HI}} = 1.38 \pm 0.14 \times 10^9 M_{\odot}$.

The integrated fluxes and the corresponding HI masses of the five components are listed in Table 1. The errors include both the rms and the calibration uncertainties (10%; Jiang et al. 2020). The latter are the dominant contributor of the errors in all cases.

4. Neighboring Galaxies in the SQ Field

HI emission of six neighboring galaxies are detected in the SQ field. They are identified in Figure 1 and Figure 3, and listed in Table 2. We also show the spectra in Figure 4. These are low-mass late-type galaxies with radial velocities in the range of 5700–6800 km s^{-1} . Among them, Anon 8 and Anon 9, named following the convention in the literature (Shostak et al. 1984; Williams et al. 2002), are new detections of this work. Anon 2 and Anon 4 were detected in previous observations (Shostak et al. 1980; Williams et al. 2002), and the FAST detections of NGC 7320a and Anon 7 were reported by Xu et al. (2022). For Anon 2 and Anon 4, the HI velocities measured by FAST are consistent with those measured by VLA within 1σ , and the values of M_{HI} by FAST are 0.1 dex and 0.2 dex above the VLA measurements, respectively, after the adjustments for the different

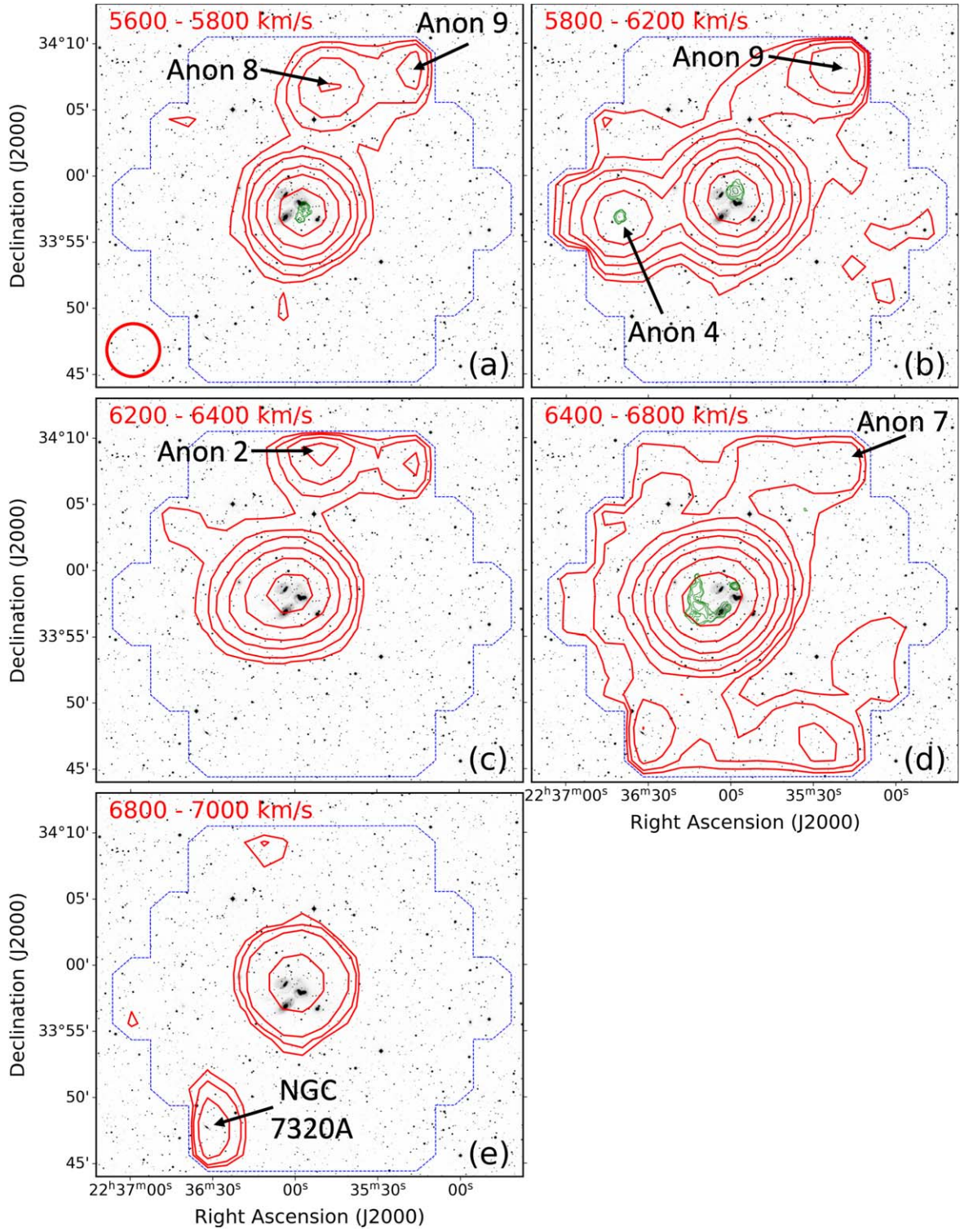


Figure 3. Contour maps of the integrated flux of the five kinematical components (see Figure 2) overlotted on an r -band image. The red contour levels are $[4, 8, 16, 32, 64, \dots] \times \sigma$, where $\sigma = \sqrt{\Delta v / 20 \text{ km s}^{-1}} \times 4.2 \times 10^{16} \text{ cm}^{-2}$, and the velocity range of each component is provided in the corresponding panel. Marked on the maps are also the neighboring galaxies detected by the FAST observations (see Section 4). The red circle at the bottom-left corner of panel (a) shows the angular resolution of the contour maps ($\text{FWHM} = 4''.0$). The green contours in panels (a), (b), and (d) represent the VLA moment-0 maps in velocity ranges of $5597\text{--}5789 \text{ km s}^{-1}$, $5959\text{--}6068 \text{ km s}^{-1}$, and $6475\text{--}6755 \text{ km s}^{-1}$, respectively. The contours levels are $5.8, 12, 18, 23, 29, 44, 58, \text{ and } 73 \times 10^{19} \text{ cm}^{-2}$ for a synthesized beam of $19''.4 \times 18''.6$.

H_0 values adopted (Williams et al. 2002 assumed $H_0 = 75 \text{ km s}^{-1} \text{ Mpc}^{-1}$ whereas we assume $H_0 = 70 \text{ km s}^{-1} \text{ Mpc}^{-1}$).

Listed in Table 2 are also the optical counterparts of these neighboring galaxies, which are identified in the SDSS images with two criteria: (1) offset $< 1''.5$ and (2) $r < 20$ mag

(corresponding roughly to $M_* > 10^7 M_\odot$). In order to confirm their correspondence to the HI detections, we carried out long slit spectroscopic observations using the Lijiang 2.4 meter telescope for these optical sources (Appendix B). Five sources, including NGC 7320a reported by Xu et al. (2022), are detected with their

optical redshifts consistent with the HI velocities. Only the counterpart of Anon 7 is undetected spectroscopically. Anon 7 is very close to the bright background radio source B2 2233+33 (R.A. = 22^h35^m17^s.7, decl. = 34^d07^m49^s), with an offset of only 0.4. Given the very high continuum flux density of B2 2233+33A ($f_{1.4\text{GHz}} = 159.4 \pm 4.8$ mJy; Condon et al. 1998), which is about 100 times the peak HI flux density of Anon 7, we cannot rule out the possibility that Anon 7 is a pseudo detection due to artifacts associated with B2 2233+33A. The optical redshifts and the stellar masses of the confirmed optical counterparts are presented in Table 2. The stellar masses are derived using the SDSS photometric data, the optical redshifts, and the code FASTPP¹⁵ (Kriek et al. 2009). The Chabrier initial mass function (Chabrier 2003) and the stellar population models of Bruzual & Charlot (2003) are adopted.

5. Discussion

5.1. HI Deficiency of Compact Groups

It has been well established that spiral galaxies in compact groups of galaxies are deficient in HI gas content (see the reviews in Verdes-Montenegro et al. 2001; Jones et al. 2023). The VLA study of Hickson compact groups (HCGs) of Verdes-Montenegro et al. (2001) show that many of them have a substantial amount of HI gas in the intragroup medium outside the member galaxies, and it is most likely that the intragroup HI is stripped gas from the spiral galaxies in the groups. However, Verdes-Montenegro et al. (2001) found that the HCGs are still HI deficient even after including the intragroup HI, with a mean HI deficiency of $\text{Def}_{\text{HI}} = 0.40 \pm 0.07$. The HI deficiency is defined by the equation $\text{Def}_{\text{HI}} = \log(M_{\text{HI, predicted}}) - \log(M_{\text{HI, observed}})$, where $M_{\text{HI, predicted}}$ is the sum of the predicted HI mass of individual spiral galaxies in a group, and the prediction is based on the optical luminosities and the morphologies. Verdes-Montenegro et al. (2001) proposed that the HI deficiency of HCGs is mainly due to the phase transition of the atomic gas in the intragroup medium during the evolution of compact groups. The GBT survey of HCGs by Borthakur et al. (2010) found a lower HI deficiency (with a mean $\text{Def}_{\text{HI}} = 0.20$), due both to the higher surface brightness sensitivity of GBT and the recovery of the missing fluxes in the VLA observations. SQ (also known by the name of HCG 92), as an archetype HCG, has all of its spiral members free of HI gas in their disks and its HI is exclusively detected in the intragroup medium (Shostak et al. 1980; Williams et al. 2002). Verdes-Montenegro et al. (2001) found a $\text{Def}_{\text{HI}} = 0.49$ for SQ, which was reduced to a $\text{Def}_{\text{HI}} = 0.28$ by Borthakur et al. (2010). In this work, we found 1.7 times more HI than the GBT observations of Borthakur et al. (2015) and 2.4 times of that of Borthakur et al. (2010), thus SQ is not HI deficient anymore. The difference between our results and those of Borthakur et al. (2015) cannot be explained by the calibration uncertainties, which are at the 10% level for both the FAST and GBT observations. A careful inspection of Figure 2, where we compare the FAST spectrum with that of Borthakur et al. (2015), reveals that our FAST observations detected significantly more HI in the 6300 and 6900 components, namely in the wings on the two sides of the 6600 km s⁻¹ peak. Because of the lower sensitivity of the GBT observations, these contributions (mainly due to low column density, diffuse HI) were missed by Borthakur et al. (2015). In line with the results of Borthakur et al. (2010), our FAST results further

Table 1
HI Kinematical Components of SQ

Name	Velocity Range (km s ⁻¹)	Integrated Flux ^a (Jy km s ⁻¹)	M_{HI} ($\times 10^9 M_{\odot}$)
5700	5600–5800	1.46 ± 0.15	2.49 ± 0.25
6000	5800–6200	5.01 ± 0.50	8.52 ± 0.85
6300	6200–6400	1.76 ± 0.18	2.99 ± 0.30
6600	6400–6800	11.42 ± 1.14	19.45 ± 1.95
6900	6800–7000	0.83 ± 0.08	1.37 ± 0.14
total	5600–7000	20.46 ± 2.05	34.86 ± 3.49

Note.

^a Errors include the rms and the calibration uncertainty (10%).

demonstrate that most of (or even all of) the missing HI in compact groups is in low-density diffuse gas. Namely, instead of transforming to ionized gas, the low-density diffuse HI is persistent as neutral gas in the intragroup medium during the group evolution. It is worth noting that the diffuse HI gas discussed here is different from the low-density HI gas in the diffuse feature discussed by Xu et al. (2022); the former is measured within the central aperture in Figure 1 and the latter is outside the aperture. Xu et al. (2022) found that the mass of the HI gas in the diffuse feature is only $\sim 3\%$ of the HI mass of SQ and is therefore too low to affect the HI deficiency index of SQ significantly.

5.2. Anon 4 and the 6000 Component

One of the possible scenarios proposed by Xu et al. (2022) for the formation of the large diffuse feature in the 6600 component (Figure 3) is that, like the large Leo Ring (Michel-Dansac et al. 2010), the diffuse feature could be the product of a high-speed head-on collision between an unknown old intruder and one of the core members of SQ (i.e., NGC 7319, NGC 7318a, and NGC 7317). In this scenario, the collision triggers an expanding density wave that pushes gas in an extended HI disk of the target galaxy outwards to form a very large ring, of which the diffuse feature is the high-density part. A candidate for such an intruder could be Anon 4 ($v = 6057$ km s⁻¹), which has a relative radial velocity of about 600 km s⁻¹ and a projected distance of approximately 0.2 Mpc from the SQ center. If the relative transverse velocity is about 200 km s⁻¹, it would have taken approximately 1 Gyr for Anon 4 to move to its current position after the collision. If this scenario is true then it is conceivable that the 6000 component of the HI emission in the debris field of SQ is due to stripped gas from Anon 4 when it passed through the group center. In order to check this hypothesis we make a P - V plot along the line connecting Anon 4 and the center of the 6000 component (Figure 5). The plot shows that the 6000 component (the emission around the position of $x = 0$ and velocity = 6000 km s⁻¹) has about the same velocity as Anon 4 (the emission around $x = -2'$), but there is no connection between the two emissions. This does not confirm any relationship between the 6000 component and Anon 4. Meanwhile, in the P - V plot, there is a spur of the 6600 component toward Anon 4. The lower-density gas between 6200 and 6400 km s⁻¹ (i.e., the 6300 component) has a similar (albeit weaker) trend. Compared to its counterparts in the 6000 and 6600 components, the central source of the 6300 component (Figure 3(c)) is slightly stretched toward the east, making its contours slightly elongated in the east–west direction (Figure 3). These trends might be suggestive of a tidal influence of Anon 4 on the HI gas in the debris field.

¹⁵ <https://github.com/cschreib/fastpp>

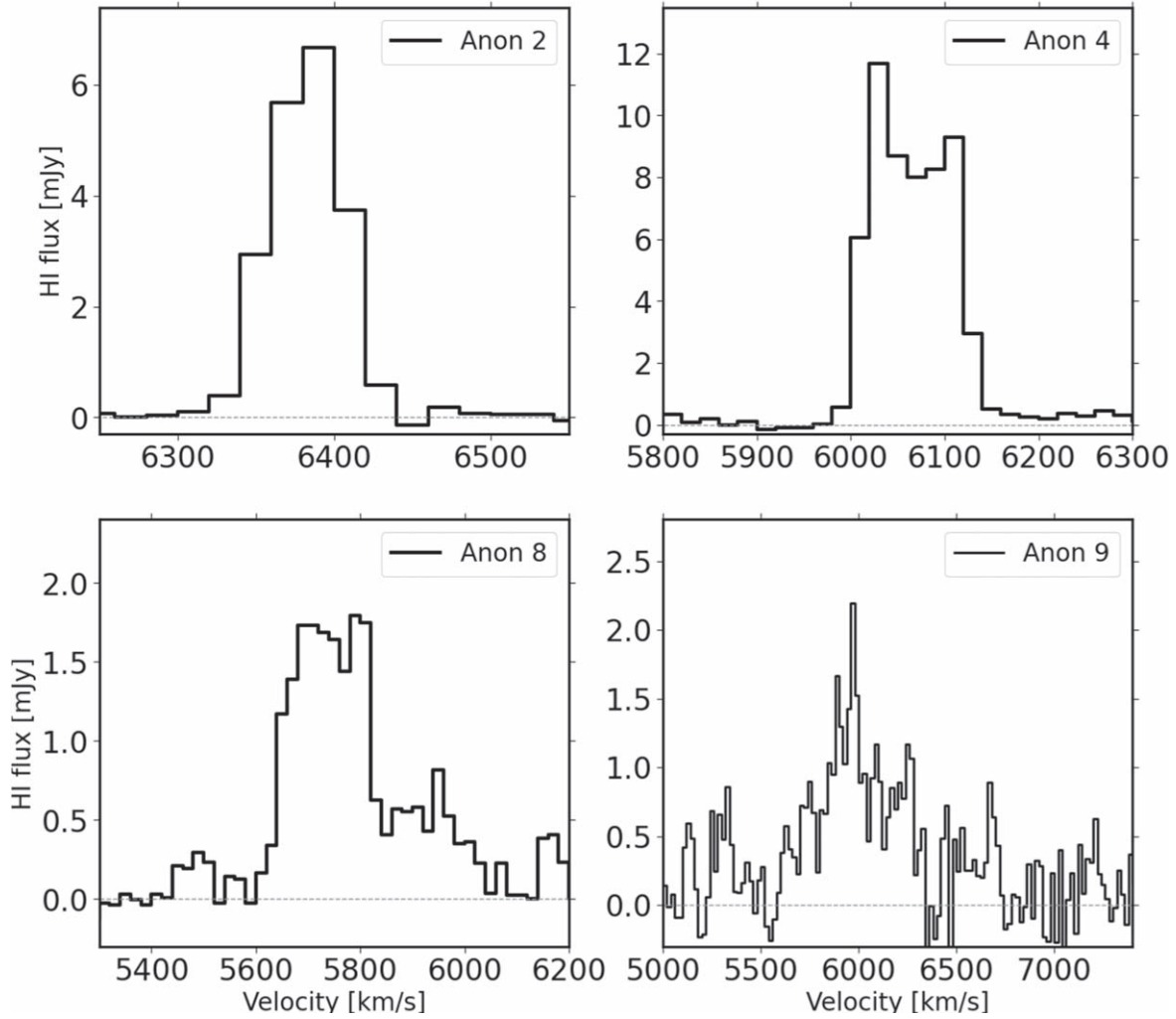


Figure 4. H I spectra of four neighboring galaxies. The dash gray lines show the position of zero flux. H I spectra of NGC 7320a and Anon 7 are presented in Xu et al. (2022).

Table 2
Neighboring Galaxies Detected by the FAST Observations

ID	R.A. J2000	Decl. J2000	H I Velocity (km s ⁻¹)	log($M_{\text{H I}}/M_{\odot}$) (log(M_{\odot}))	Optical ID	log(M_{*}/M_{\odot}) ^a (log(M_{\odot}))	Optical Velocity ^b (km s ⁻¹)	References ^c
Anon 2	22:35:50.7	+34:09:30	6391 ± 8	8.90 ± 0.04	SDSSJ223550.70+340930.8	8.58	6325 ± 140	1, 2
Anon 4	22:36:40.9	+33:56:54	6075 ± 13	9.30 ± 0.04	SDSSJ223640.85+335654.5	8.62	6089 ± 141	1, 2
Anon 7 ^d	22:35:19.3	+34:08:00	6654 ± 16	8.34 ± 0.10	SDSSJ223526.26+340837.9	3
Anon 8	22:35:47.5	+34:06:48	5789 ± 20	8.88 ± 0.04	SDSSJ223547.54+340648.1	9.46	5625 ± 151	1
Anon 9	22:35:22.7	+34:08:03	5976 ± 38	9.01 ± 0.05	SDSSJ223526.26+340837.9	8.12	5886 ± 145	1
NGC 7320a ^e	22:36:32.2	+33:47:46	6702 ± 24	8.80 ± 0.04	NGC 7320a	10.08	6729 ± 59	3

Notes.

^a Stellar mass derived from SDSS photometry and optical redshift.

^b Optical velocity in the LSR reference frame.

^c References: (1) This work; (2) Williams et al. (2002); and (3) Xu et al. (2022).

^d H I data taken from Xu et al. (2022); uncertain optical identification.

^e H I data and optical velocity taken from Xu et al. (2022).

5.3. Long History of Interactions in SQ

Moles et al. (1997) proposed a comprehensive picture for the interaction history of SQ based on a “two-intruders” scenario (also see Sulentic et al. 2001): an old intruder (NGC 7320c) stripped most of the gas from group members, and a new

intruder (NGC 7318b) is currently colliding with this gas and triggering the large-scale shock. The “old intruder” passed the core of SQ twice, once $\sim 5 - 7 \times 10^8$ yr ago and pulled out the outer tail (also known as “old tail”), and another about 2×10^8 yr ago, triggering the inner tail (“young tail”). Xu et al. (2005), based on newer observations, argued that it is more

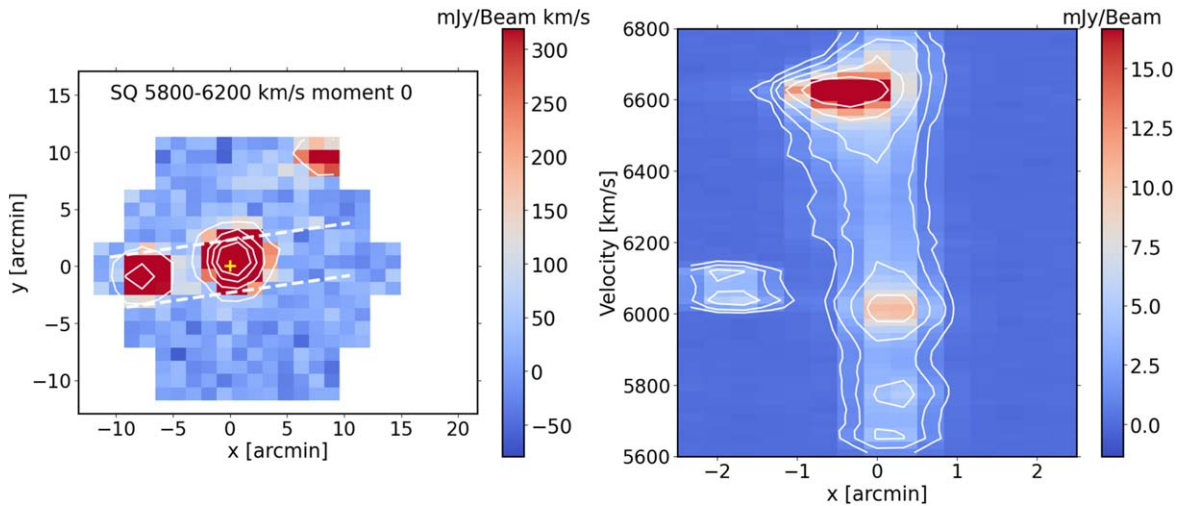


Figure 5. Left: contours and false color map of the 6000 component. The dashed white lines delineate the stripe within which the data of the P - V plot (in the right panel) are taken. The yellow cross marks the sky position of $x = 0$ in the P - V plot, whose coordinates are $22^{\text{h}}36^{\text{m}}00^{\text{s}}.8 + 33^{\text{d}}57^{\text{m}}47^{\text{s}}$. The width of the stripe is $5'$ and the position angle is $\text{P.A.} = 99^\circ$. Right: P - V plot. The contours start from 1 mJy beam^{-1} (beamwidth = $2.9'$) with an increment of a factor of 2.

likely that the inner tail is triggered by NGC 7318a, which has a closer projected distance to NGC 7319 than NGC 7320c. However, the simulations of Renaud et al. (2010) and Hwang et al. (2012) found that, if indeed the inner tail is generated later in a different encounter, it is very difficult for the outer tail to survive the strong tidal influence during the second passage. Instead, Hwang et al. (2012) concluded that it is most likely that the two tails are triggered by the same passage of NGC 7320c from a very close vicinity to NGC 7319 about 9×10^8 years ago. The fiducial model of Hwang et al. (2012) can reasonably reproduce the positions of the galaxies involved in the encounter between NGC 7319 and NGC 7320c and that between NGC 7318a and NGC 7318b, and the locations and the orientations of the inner and older tails. However, it cannot reproduce the overall HI distribution in SQ, and in particular it predicts that NGC 7319 and NGC 7318b still retain most of their gas, in contradiction with the observations. For NGC 7318b, the fiducial model of Hwang et al. (2012) assumes that it has a relative radial velocity with NGC 7318a of $\Delta v \sim 300 \text{ km s}^{-1}$, which is significantly lower than the observed value ($\Delta v \sim 900 \text{ km s}^{-1}$). This may cause an underestimate of the strength of the density waves triggered by the head-on collision and result in less gas removal from NGC 7318b. For NGC 7319, the assumption of the initial gas distribution as in a normal disk is unrealistic. As argued by Xu et al. (2022), the diffuse HI feature attached to the south edge of the debris field was most likely produced by an interaction between a core galaxy of SQ and an earlier intruder (e.g., NGC 7320a or Anon 4) prior to the invasion of NGC 7320c. If the involved core galaxy were NGC 7319, then its gas disk had been already distorted when NGC 7320c arrived. Alternatively, NGC 7319 could have had been involved in a collision with the elliptical galaxy NGC 7317, which seems to be linked to NGC 7319 by a diffuse optical halo (Moles et al. 1997; Duc et al. 2018). The recently published JWST MIRI images of SQ in the JWST Early Release Observations (Pontoppidan et al. 2022) show some peculiar features for NGC 7319 in the $7.7 \mu\text{m}$ band in incredible detail, which are presumably dominated by the emission of polycyclic aromatic hydrocarbon molecules. These features do not look like any tidal arms/tails at all, but are very similar to the spokes in a ring galaxy which are

triggered by a head-on collision with an intruder galaxy (e.g., those in the Cartwheel Galaxy; Renaud et al. 2018). The rather high molecular gas content and very low SFR in the disk of NGC 7319 (Gao & Xu 2000; Xu et al. 2005; Yttergren et al. 2021) correspond to a very low star formation efficiency, similar to the situation in Arp 142, a ring galaxy involved in a head-on collision previously (Xu et al. 2021). On the other hand, it is not clear whether the spoke-like features seen in the JWST images were indeed produced by a head-on collision ~ 1 Gyr ago, because according to the current theory the effects of such collisions fade away in a few $\times 10^8$ yr (Renaud et al. 2018). And even if they were, could they survive the tidal force during the subsequent passage of NGC 7320c? These question can only be answered in future simulations.

5.4. Origin of the Diffuse HI Feature

Given its spatial and kinematical connections to the debris field produced by interactions among core members of SQ and by collisions with numerous intruders, Xu et al. (2022) argued that the diffuse feature was most likely due to gas ejected from one of the core galaxies during an interaction with an early intruder (plausibly NGC 7320a or Anon 4) more than 1 Gyr ago. Xu et al. (2022) ruled out the hypothesis that the diffuse feature is merely a collection of unresolved “dark” or “almost dark” galaxies (Leisman et al. 2021) on the grounds that it is very extended ($\sim 0.5 \text{ Mpc}$) and has a narrow velocity range ($\Delta v_{20} = 160 \text{ km s}^{-1}$). However, there are other possibilities.

First of all, it is possible that the diffuse feature is a tidal tail pulled out from the neighboring spiral galaxy NGC 7320a instead of from a core member of SQ. The diffuse HI feature is right next to NGC 7320a, and its radial velocity ($v = 6633 \text{ km s}^{-1}$) is very close to that of NGC 7320a ($v = 6702 \text{ km s}^{-1}$). The simulations of Duc & Bournaud (2008) suggested that high-speed encounters (relative velocities of $\sim 1000 \text{ km s}^{-1}$) between two galaxies of nearly equal mass can produce long HI streams similar to this diffuse feature. Indeed there is an early-type galaxy, KAZ 295, at the other end of the diffuse feature opposite to NGC 7320a. Our new optical spectroscopy finds a redshift velocity of 6555 km s^{-1} for the galaxy (see Appendix B), confirming it to be at about the same distance of NGC 7320a. Its stellar mass estimated from the SDSS photometry is $M_* = 10^{9.71} M_\odot$, which is slightly lower than

that of NGC 7320a ($M_* = 10^{10.08} M_\odot$). In analog to the simulation of Duc & Bournaud (2008), KAZ 295 may have a high transverse velocity relative to NGC 7320a, and the encounter between the two may have pulled a long HI stream from NGC 7320a that is identified by us as the diffuse feature. However there are some inconsistencies which cast doubts on the analogy. The case simulated by Duc & Bournaud (2008) is for two massive galaxies of $M_* > 10^{11} M_\odot$, and NGC 7320a and KAZ 295 are low-mass galaxies of $M_* \sim 10^{10} M_\odot$. Also the simulated HI stream is only ~ 200 kpc whereas the length of the diffuse feature is ~ 500 kpc. Whether the putative interaction between the two low-mass galaxies can trigger the formation of an HI feature as long as 500 kpc needs to be investigated by future studies.

Another possibility is that the diffuse feature might be due to cold gas accretion by the SQ group from the intergalactic medium (IGM) in the large-scale filaments. The diffuse feature locates at the bottom of the FAST map and may well reach beyond the map. In the large-scale environment, SQ is in a rather high-density region embedded within one of the main filaments of the Perseus supercluster (Gregory et al. 2000). Tammann (1970) suggested that SQ is perhaps part of the Zwicky Cluster at $22^{\text{h}}31^{\text{m}}2+37^{\circ}32'$ (Zwicky & Kowal 1968). That explains why there are many neighboring galaxies in the SQ field in a relatively large velocity range (5600–7000 km s⁻¹), and why SQ has been intruded many times in its past history.

The smooth accretion of intergalactic gas from the surrounding filaments is a major growth mode for galaxy clusters and groups (Walker et al. 2019). The cold intergalactic gas, which is mostly ionized and is $\sim 15\%$ of the IGM in the filaments (Cantalupo et al. 2012), has been detected by observations of Ly α emission and absorption (Cantalupo et al. 2014; Finley et al. 2014; Umehata et al. 2019), and by studies on the cross-correlations between neutral hydrogen (HI) 21 cm intensity maps and galaxy surveys (Chang et al. 2010; Masui et al. 2013). On the other hand, there is no confirmed detection of the HI 21 cm line emission of the filaments in the literature. Although the “HI bridge” detected in the intergalactic space between M31 and M33, which has a characteristic column density of $N_{\text{HI}} \sim 10^{18} \text{ cm}^{-2}$, was first interpreted as the product of condensation within an intergalactic filament (Braun 2004; Lockman et al. 2012; Wolfe et al. 2016), later simulations by Tepper-García et al. (2022) suggest that it is more likely a tidal feature triggered by a close encounter between the two galaxies ~ 6.5 Gyr ago. Indeed, theoretical models predicted very low neutral HI column density of the filaments, with a mean $N_{\text{HI}} \sim 10^{14} \text{ cm}^{-2}$ for the total and a mean $N_{\text{HI}} \sim 10^{16} \text{ cm}^{-2}$ for the brightest 10% of the filaments (Kooistra et al. 2019). This is significantly lower than the characteristic HI column density of the diffuse feature ($N_{\text{HI}} \sim 7 \times 10^{17} \text{ cm}^{-2}$; Xu et al. 2022). Nevertheless, this does not completely reject the accretion hypothesis for the origin of the diffuse feature. Future HI observations exploring the regions beyond the south boundary of our FAST map, preferably with even higher sensitivity, will provide crucial constraints to this hypothesis.

6. Summary

HI mapping observations were carried out using the FAST 19-beam receiver. The observations cover a sky region of size of $\sim 30' \times 30'$ around SQ with an angular resolution of 2.9 and a sampling that satisfies the Nyquist criterion. The smoothed sensitivity of the data (resolution = $4'$) reaches

$1\sigma = 4.3 \times 10^{16} \text{ cm}^{-2}$ for 20 km s⁻¹ channels. The discovery of a large HI structure of radial velocity of 6633 km s⁻¹ was presented in Xu et al. (2022). In this paper, we report the following new results:

1. The HI spectrum of SQ covers a wide velocity range between 5600 and 7000 km s⁻¹, with an integrated flux of $20.5 \pm 2.1 \text{ Jy km s}^{-1}$. The corresponding HI mass is $M_{\text{HI}} = 3.48 \pm 0.35 \times 10^{10} M_\odot$ (for a comoving distance of 85 Mpc). This is significantly higher than previous measurements from VLA and GBT observations (Verdes-Montenegro et al. 2001; Williams et al. 2002; Borthakur et al. 2010, 2015) and indicates that, when including the HI gas in the intragroup medium, SQ is not HI deficient.
2. The HI emission of SQ can be divided into five kinematical components: 5700 component (5600–5800 km s⁻¹), 6000 component (6000–6200 km s⁻¹), 6300 component (6200–6400 km s⁻¹), 6600 component (6400–6800 km s⁻¹), and 6900 component (6800–7000 km s⁻¹). Whereas the 5700, 6000, and 6600 components have been detected previously, the 6300 and 6900 components were undetected or only marginally detected in previous observations due to inadequate sensitivity. The net HI mass of the 6300 and 6900 components is $5.71 \pm 0.42 \times 10^{10} M_\odot$, which is $16.4\% \pm 1.6\%$ of the total HI of SQ.
3. The HI emissions of six neighboring galaxies are detected in the SQ field. These include NGC 7320a, Anon 2, Anon 4, Anon 7, Anon 8, and Anon 9. These are low-mass late-type galaxies with radial velocities in the range of 5700–6800 km s⁻¹. Among them, Anon 2 and Anon 4 were detected in previous observations (Shostak et al. 1980; Williams et al. 2002), and the FAST detections of NGC 7320a and Anon 7 were reported by Xu et al. (2022). We obtain the optical redshifts for optical counterparts of Anon 2, Anon 4, Anon 8, and Anon 9, which are consistent with the HI radial velocities.
4. The FAST observations provide new evidence for a complex and long history of SQ, particularly before the formation of the inner and outer tails. The newly discovered diffuse feature is most likely due to a gas ejection from one of the core galaxies during an interaction with an early intruder (NGC 7320a or Anon 4) more than 1 Gyr ago. However the possibilities that the diffuse feature is an HI stream pull out from the neighboring low-mass spiral NGC 7320a by a high-speed encounter with another low-mass galaxy (KAZ 295), and that the diffuse feature might be due to cold gas accretion by the SQ group from the IGM in the large-scale filaments, warrant further investigations.

Acknowledgments

We thank the referee for careful reading and constructive suggestions. This work is supported by the National Key R&D Programme of China No. 2017YFA0402704 and National Natural Science Foundation of China (NSFC) No. 11873055 and sponsored (in part) by the Chinese Academy of Sciences (CAS) through a grant to the CAS South America Center for Astronomy. C.K.X. acknowledges NSFC grant No. 11733006. C.C. acknowledges NSFC grant No. 11803044 and 12173045. We acknowledge the science research grants from the China Manned Space Project with No. CMS-CSST-2021-A05. N.-Y.T. is sponsored by

Zhejiang Lab Open Research Project (No. K2022PE0AB01), Cultivation Project for FAST Scientific Payoff and Research Achievement of CAMS-CAS, National key R&D program of China under grant No. 2018YFE0202900 and the University Annual Scientific Research Plan of Anhui Province (No. 2022AH010013). Y.S.D. acknowledges support from the National Key R&D Program of China for grant No. 2022YFA1605300 and the National Nature Science Foundation of China (NSFC) grants No. 12273051 and 11933003; J.-S.H. acknowledges NSFC grant No. 11933003. U.L. acknowledges support from project PID2020-114414GB-100, financed by MCIN/AEI/10.13039/501100011033, from project P20_00334 financed by the Junta de Andalucía and from FEDER/Junta de Andalucía-Consejería de Transformación Económica, Industria, Conocimiento y Universidades/Proyecto A-FQM-510-UGR20. F.R. acknowledges support from the Knut and Alice Wallenberg Foundation. This work made use of data from FAST, a Chinese national mega-science facility built and operated by the National Astronomical Observatories, CAS. We thank P. Jiang, L. Hou, C. Sun, and other FAST operation team members for support in the observations and data reduction, and Y. Huang and K.-X. Lu for helping with the optical spectroscopic observations. C.C. appreciates helpful comments about the usage of matplotlib from Dr. Wenda Zhang. The support of the staff of the Lijiang 2.4 m telescope is acknowledged. Funding for the Lijiang 2.4 m telescope has been provided by the CAS and the People's Government of Yunnan Province. This research has made use of the NASA/IPAC Extragalactic Database,

which is operated by the Jet Propulsion Laboratory, California Institute of Technology, under contract with the National Aeronautics and Space Administration.

Facilities: FAST (19-Beam Receiver) and the Lijiang 2.4 m telescope (YFOSC).

Software: astropy (Astropy Collaboration et al. 2013, 2018), Source Extractor (Bertin & Arnouts 1996), pvextractor (Ginsburg et al. 2016), and Radio Astronomy Tools in Python (Ginsburg et al. 2015).

Appendix A H I Channel Maps

The Figure A1 presents channel maps of the FAST observations, covering the velocity range between 5500 and 7080 km s⁻¹ with 80 channels of width $\Delta v = 20$ km s⁻¹. In each channel map, contours of the H I emission (with smoothed angular resolution of 4') are overlaid on the inverted gray-scale map of a deep CFHT MegaCam *r*-band image (Duc et al. 2018). The contours start from $N_{\text{HI}} = 1.3 \times 10^{17}$ cm⁻² (at the 3σ level) with increments of a factor of 2. The central source associated with the SQ proper is detected in most channels. The diffuse feature reported in Xu et al. (2022) is visible close to the bottom of the field in channels centered at $v = 6620, 6640,$ and 6660 km s⁻¹. Several neighboring galaxies are also detected in different channels across the velocity range, which are discussed in detail in Section 4.

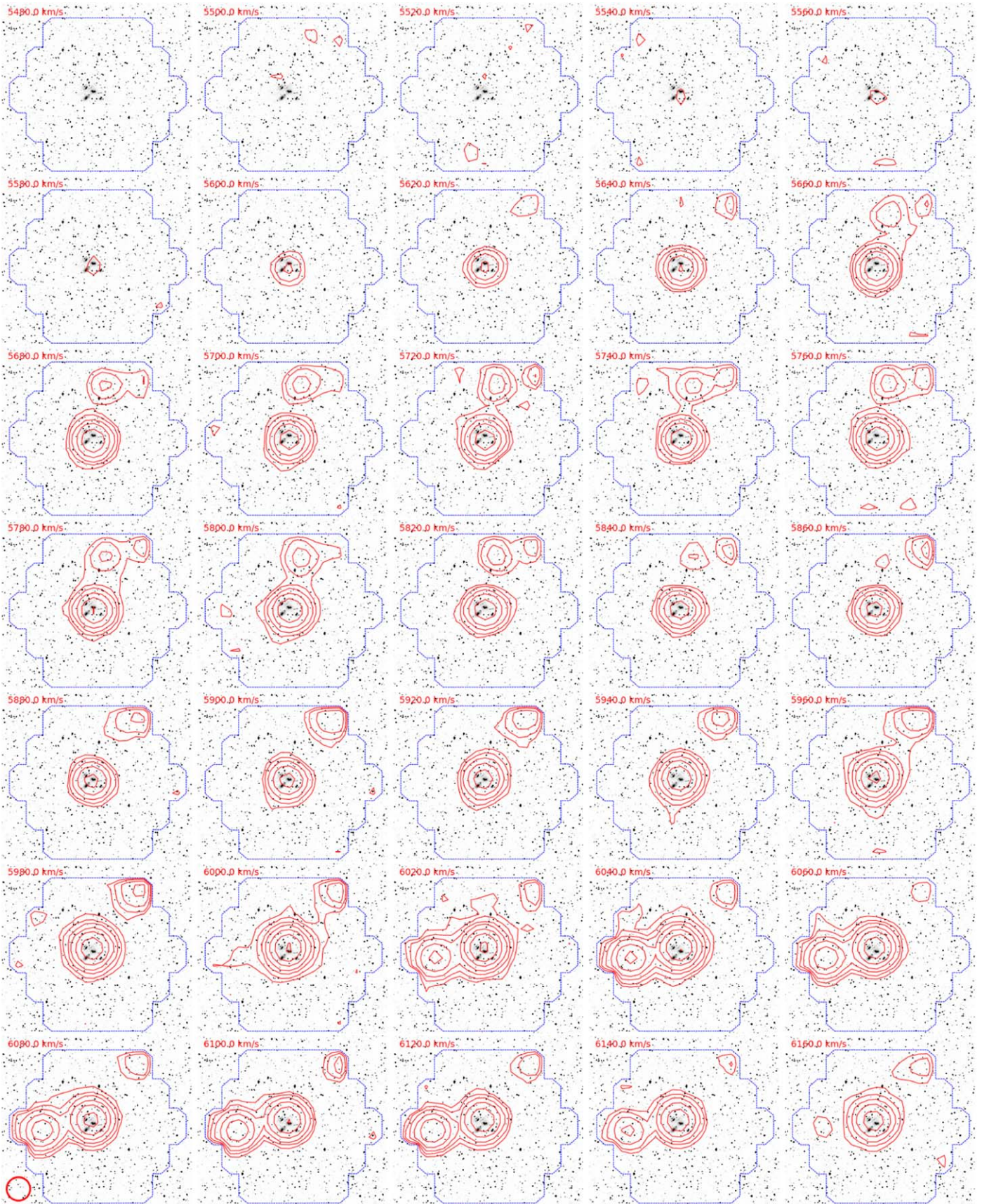


Figure A1. (Top) FAST H I channel maps (contours) overlotted on a CFHT *r*-band image (Duc et al. 2018). The channel maps cover the velocity range of 5480–7040 km s⁻¹ with a channel width of 20 km s⁻¹. The contour levels are [3, 6, 12, 24, 48, 96...] × 4.2 × 10¹⁶ cm⁻². The blue boundaries delineate the FAST coverage. The small red circle at lower left corner of the first map in the last row shows the angular resolution of the H I channel maps (FWHM = 4'). (Middle) and (bottom) Contours of the H I channel maps overlotted on the *r*-band image.

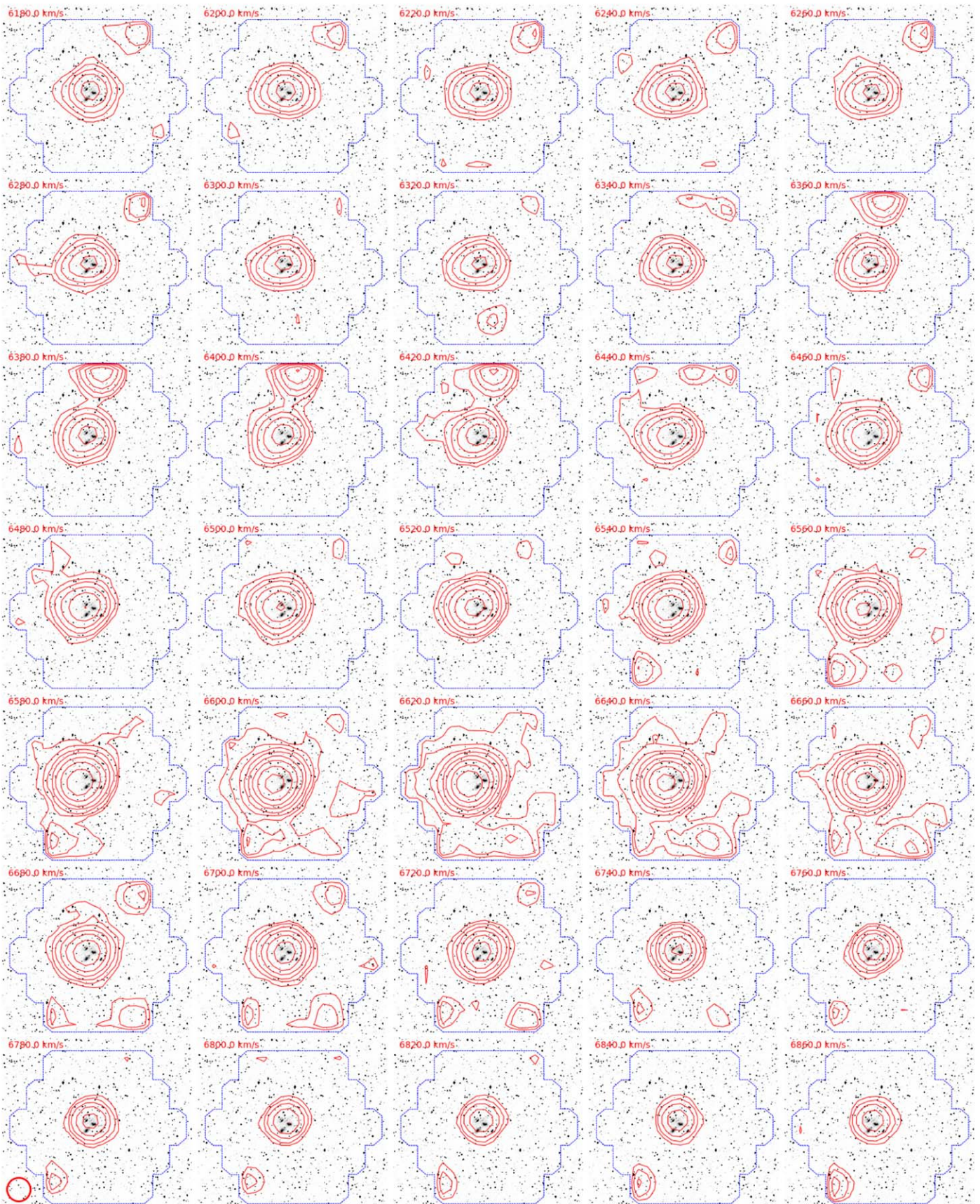


Figure A1. (Continued.)

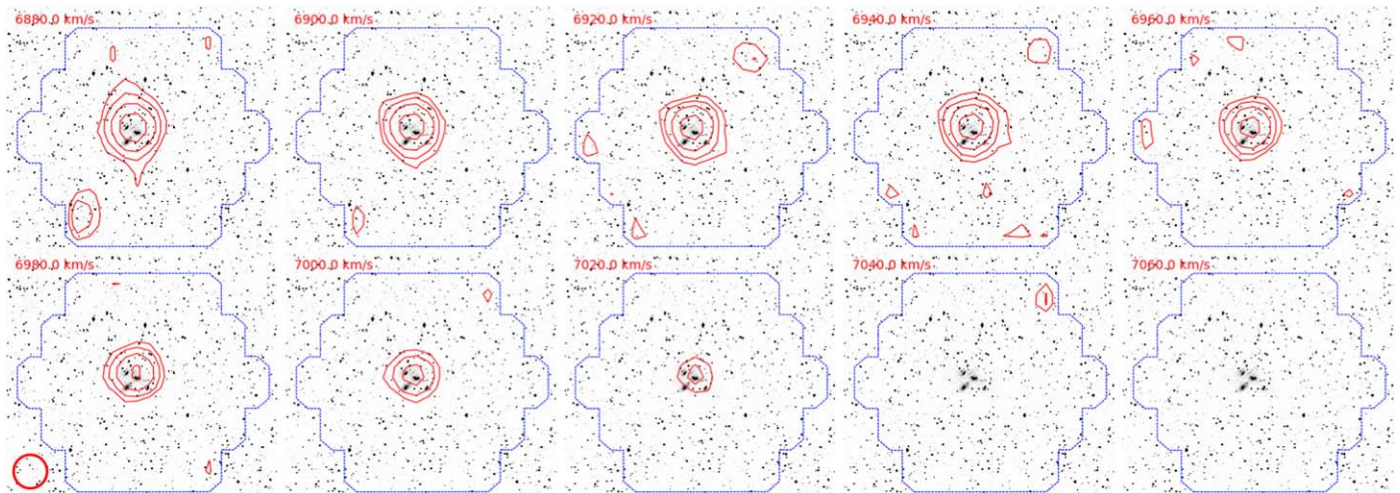


Figure A1. (Continued.)

Appendix B Optical Spectroscopic Observations of Neighboring Galaxies

We performed long slit spectroscopic observations for the optical counterparts of Anon 2, Anon 4, Anon 7, Anon 8, and Anon 9, and for the optical galaxy KAZ 295, using the Lijiang 2.4 m telescope on 2022 October 30–31 and December 14. A slit of $1''.8$ width was chosen, which matches the seeing. We used the G14 grating with a wavelength coverage from 3500 to 7000 and a resolution of about 1000, which can help us to cover bright emission lines such as $H\alpha$, [O III], as well as the [O II] and Ca II H, K lines at bluer wavelengths. The exposure

time is about 2 hr for each target. We reduced the long slit spectra using a standard IRAF script. An HeNe lamp was used for wavelength calibration. However, bright lines of the lamp spectra were saturated, which affected our wavelength accuracy. Thus, conservatively, we included a wavelength calibration error of $1\sigma = 3 \text{ \AA}$ (137 km s^{-1}). Since the spectra are for redshift measurements only, no flux calibration was performed. The spectra of the optical counterparts of Anon 2, Anon 4, and Anon 8, and of the optical galaxy KAZ 295, are presented in Figure B1. The spectrum of the optical counterpart of Anon 9, which is a weak detection, is presented in Figure B2. The units of the flux density (F_λ) in the figures are arbitrary.

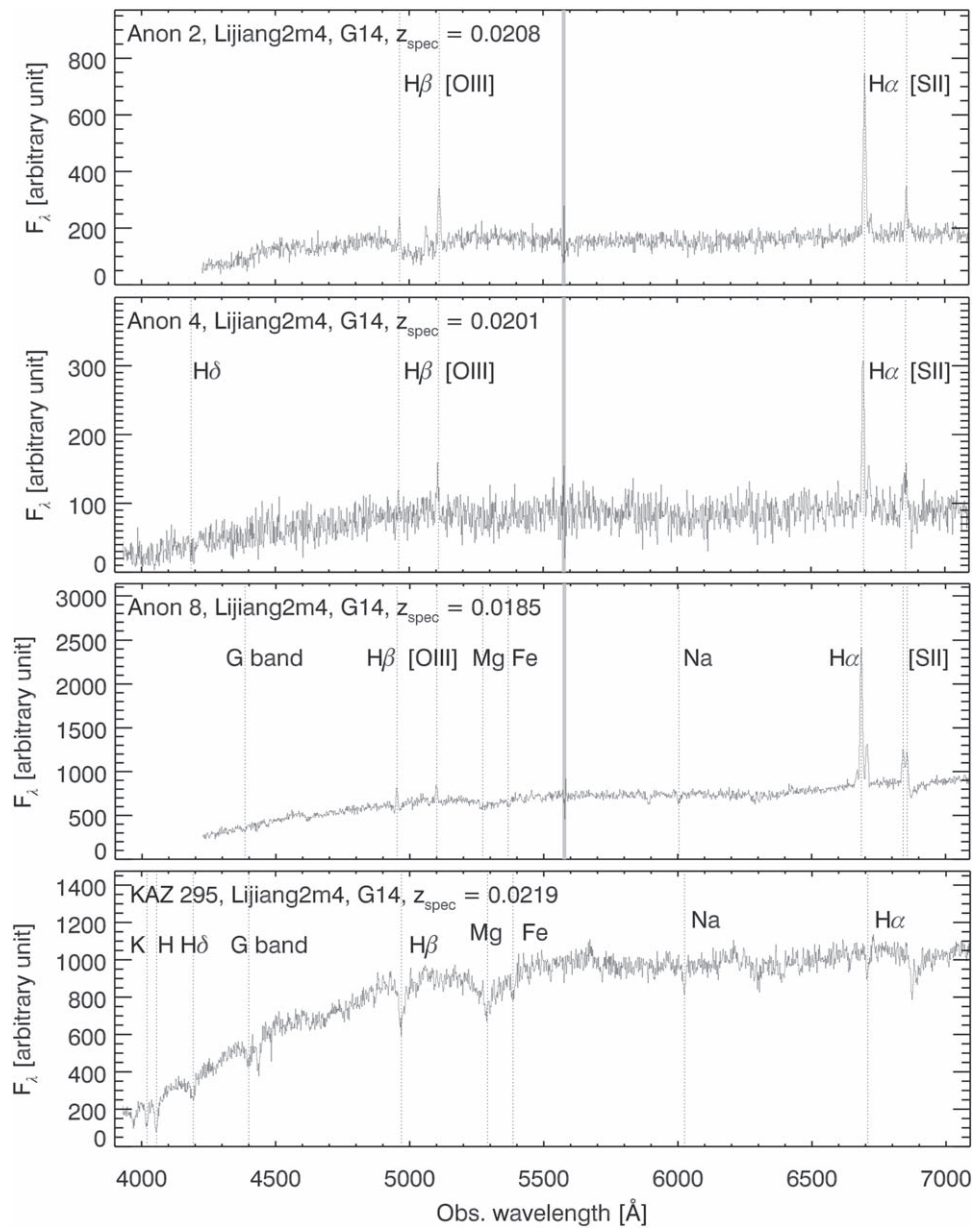


Figure B1. Optical spectra. The gray regions are contaminated by sky lines.

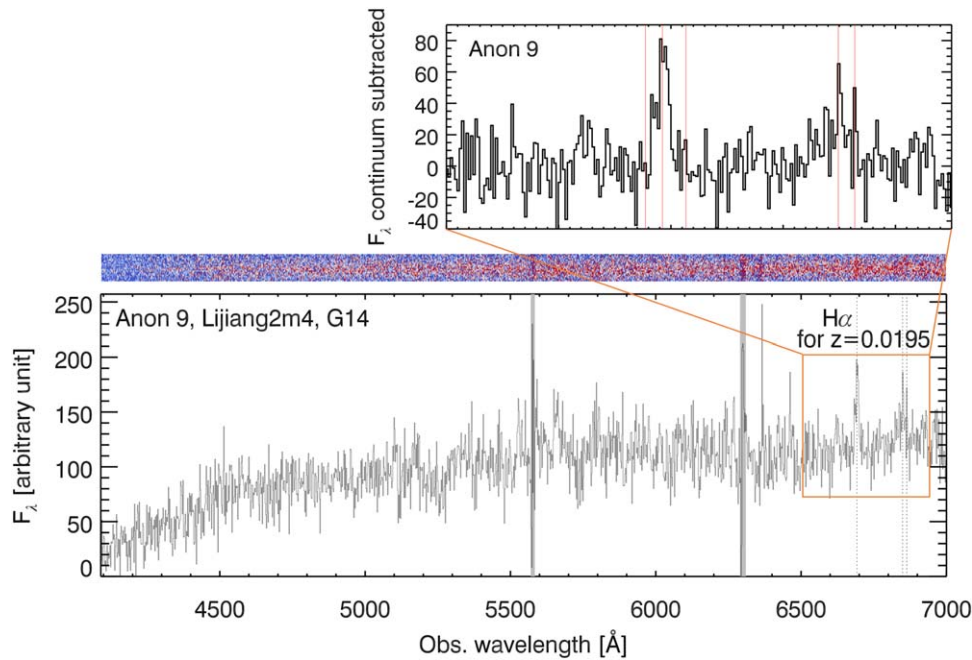


Figure B2. Top panel: continuum-subtracted spectrum of the optical counterpart of Anon 9 between 6500 and 6950 Å observed wavelength. The red lines indicate the [N II], H α , and [S II] positions at a redshift of 0.0195. Middle panel: 2D spectrum of Anon 9 with the wavelength range the same as the lower panel. Lower panel: 1D original spectrum. The dash lines show the positions of H α and [S II] at $z = 0.0195$. The gray regions are contaminated by sky lines.

ORCID iDs

Cheng Cheng <https://orcid.org/0000-0003-0202-0534>
 Cong Kevin Xu <https://orcid.org/0000-0002-1588-6700>
 P. N. Appleton <https://orcid.org/0000-0002-7607-8766>
 P.-A. Duc <https://orcid.org/0000-0003-3343-6284>
 N.-Y. Tang <https://orcid.org/0000-0002-2169-0472>
 Y.-S. Dai <https://orcid.org/0000-0002-7928-416X>
 J.-S. Huang <https://orcid.org/0000-0001-6511-8745>
 U. Lisenfeld <https://orcid.org/0000-0002-9471-5423>
 F. Renaud <https://orcid.org/0000-0001-5073-2267>
 Chuan He <https://orcid.org/0000-0003-1761-5442>
 Hai-Cheng Feng <https://orcid.org/0000-0002-1530-2680>

References

- Alatalo, K., Appleton, P. N., Lisenfeld, U., et al. 2014, *ApJ*, 795, 159
 Allen, R. J., & Hartsuiker, J. W. 1972, *Natur*, 239, 324
 Aoki, K., Ohtani, H., Yoshida, M., & Kosugi, G. 1996, *AJ*, 111, 140
 Appleton, P. N., Guillard, P., Boulanger, F., et al. 2013, *ApJ*, 777, 66
 Appleton, P. N., Guillard, P., Emonts, B., et al. 2023, *ApJ*, 951, 104
 Appleton, P. N., Guillard, P., Togi, A., et al. 2017, *ApJ*, 836, 76
 Appleton, P. N., Xu, K. C., Reach, W., et al. 2006, *ApJL*, 639, L51
 Astropy Collaboration, Price-Whelan, A. M., Sipőcz, B. M., et al. 2018, *AJ*, 156, 123
 Astropy Collaboration, Robitaille, T. P., & Tollerud, E. J. 2013, *A&A*, 558, A33
 Bertin, E., & Arnouts, S. 1996, *A&AS*, 117, 393
 Borthakur, S., Yun, M. S., & Verdes-Montenegro, L. 2010, *ApJ*, 710, 385
 Borthakur, S., Yun, M. S., Verdes-Montenegro, L., et al. 2015, *ApJ*, 812, 78
 Braun, R. 2004, *NewAR*, 48, 1271
 Bruzual, G., & Charlot, S. 2003, *MNRAS*, 344, 1000
 Cantalupo, S., Arrigoni-Battaia, F., Prochaska, J. X., Hennawi, J. F., & Madau, P. 2014, *Natur*, 506, 63
 Cantalupo, S., Lilly, S. J., & Haehnelt, M. G. 2012, *MNRAS*, 425, 1992
 Chabrier, G. 2003, *PASP*, 115, 763
 Chang, T.-C., Pen, U.-L., Bandura, K., & Peterson, J. B. 2010, *Natur*, 466, 463
 Cheng, C., Ibar, E., Du, W., et al. 2020, *A&A*, 638, L14
 Cluver, M. E., Appleton, P. N., Boulanger, F., et al. 2010, *ApJ*, 710, 248
 Cluver, M. E., Appleton, P. N., Ogle, P., et al. 2013, *ApJ*, 765, 93
 Condon, J. J., Cotton, W. D., Greisen, E. W., et al. 1998, *AJ*, 115, 1693
 Duarte Puertas, S., Iglesias-Páramo, J., Vilchez, J. M., et al. 2019, *A&A*, 629, A102
 Duc, P.-A., & Bournaud, F. 2008, *ApJ*, 673, 787
 Duc, P.-A., Cuillandre, J.-C., & Renaud, F. 2018, *MNRAS*, 475, L40
 Enßlin, T. A. 2002, *A&A*, 396, L17
 Fedotov, K., Gallagher, S. C., Konstantopoulos, I. S., et al. 2011, *AJ*, 142, 42
 Finley, H., Petitjean, P., Noterdaeme, P., & Pâris, I. 2014, *A&A*, 572, A31
 Gallagher, S. C., Charlton, J. C., Hunsberger, S. D., Zaritsky, D., & Whitmore, B. C. 2001, *AJ*, 122, 163
 Gao, Y., & Xu, C. 2000, *ApJL*, 542, L83
 Ginsburg, A., Robitaille, T., Beaumont, C., et al. 2015, in ASP Conf. Ser. 499, Revolution in Astronomy with ALMA: The Third Year, ed. D. Iono, K. Tatematsu, & L. Testi (San Francisco, CA: ASP), 363
 Ginsburg, A., Robitaille, T., & Beaumont, C. 2016, pvextractor: Position-Velocity Diagram Extractor, Astrophysics Source Code Library, ascl:1608.010
 Gregory, S. A., Tift, W. G., Moody, J. W., Newberry, M. V., & Hall, S. M. 2000, *AJ*, 119, 567
 Guillard, P., Appleton, P. N., Boulanger, F., et al. 2022, *ApJ*, 925, 63
 Guillard, P., Boulanger, F., Pineau des Forêts, G., et al. 2012, *ApJ*, 749, 158
 Hickson, P. 1982, *ApJ*, 255, 382
 Hwang, J.-S., Struck, C., Renaud, F., & Appleton, P. N. 2012, *MNRAS*, 419, 1780
 Iglesias-Páramo, J., López-Martín, L., Vilchez, J. M., Petropoulou, V., & Sulentic, J. W. 2012, *A&A*, 539, A127
 Jiang, P., Tang, N.-Y., Hou, L.-G., et al. 2020, *RAA*, 20, 064
 Jiang, P., Yue, Y., Gan, H., et al. 2019, *SCPMA*, 62, 959502
 Johnson, K. E., Hibbard, J. E., Gallagher, S. C., et al. 2007, *AJ*, 134, 1522
 Jones, M. G., Verdes-Montenegro, L., Moldon, J., et al. 2023, *A&A*, 670, A21
 Kooistra, R., Silva, M. B., Zaroubi, S., et al. 2019, *MNRAS*, 490, 1415
 Kriek, M., van Dokkum, P. G., Labbé, I., et al. 2009, *ApJ*, 700, 221
 Leisman, L., Rhode, K. L., Ball, C., et al. 2021, *AJ*, 162, 274
 Lenkić, L., Tzanavaris, P., Gallagher, S. C., et al. 2016, *MNRAS*, 459, 2948
 Lisenfeld, U., Alatalo, K., Zucker, C., et al. 2017, *A&A*, 607, A110
 Lisenfeld, U., Braine, J., Duc, P. A., et al. 2004, *A&A*, 426, 471
 Lockman, F. J., Free, N. L., & Shields, J. C. 2012, *AJ*, 144, 52
 Masui, K. W., Switzer, E. R., Banavar, N., et al. 2013, *ApJL*, 763, L20
 Michel-Dansac, L., Duc, P.-A., Bournaud, F., et al. 2010, *ApJL*, 717, L143
 Moles, M., Sulentic, J. W., & Márquez, I. 1997, *ApJL*, 485, L69
 Peterson, S. D., & Shostak, G. S. 1980, *ApJL*, 241, L1
 Pontoppidan, K. M., Barrientes, J., Blome, C., et al. 2022, *ApJL*, 936, L14
 Qian, L., Yao, R., Sun, J., et al. 2020, *Innov*, 1, 100053
 Renaud, F., Appleton, P. N., & Xu, C. K. 2010, *ApJ*, 724, 80

- Renaud, F., Athanassoula, E., Amram, P., et al. 2018, *MNRAS*, **473**, 585
- Sanders, D. B. 1996, *ARA&A*, **34**, 749
- Shostak, G. S., Gilra, D. P., Noordam, J. E., et al. 1980, *A&A*, **81**, 223
- Shostak, G. S., Sullivan, W. T. I., & Allen, R. J. 1984, *A&A*, **139**, 15
- Stephan, M. 1877, *MNRAS*, **37**, 334
- Sulentic, J. W., Rosado, M., Dultzin-Hacyan, D., et al. 2001, *AJ*, **122**, 2993
- Tammann, G. A. 1970, *ApL*, **7**, 111
- Tepper-García, T., Bland-Hawthorn, J., & Freeman, K. 2022, *MNRAS*, **515**, 5951
- Trinchieri, G., Sulentic, J., Pietsch, W., & Breitschwerdt, D. 2005, *A&A*, **444**, 697
- Umehata, H., Fumagalli, M., Smail, I., et al. 2019, *Sci*, **366**, 97
- van der Hulst, J. M., & Rots, A. H. 1981, *AJ*, **86**, 1775
- Verdes-Montenegro, L., Yun, M. S., Williams, B. A., et al. 2001, *A&A*, **377**, 812
- Walker, S., Simionescu, A., Nagai, D., et al. 2019, *SSRv*, **215**, 7
- Williams, B. A., Yun, M. S., & Verdes-Montenegro, L. 2002, *AJ*, **123**, 2417
- Wolfe, S. A., Lockman, F. J., & Pisano, D. J. 2016, *ApJ*, **816**, 81
- Xu, C., Sulentic, J. W., & Tuffs, R. 1999, *ApJ*, **512**, 178
- Xu, C. K., Cheng, C., Appleton, P. N., et al. 2022, *Natur*, **610**, 461
- Xu, C. K., Iglesias-Páramo, J., Burgarella, D., et al. 2005, *ApJL*, **619**, L95
- Xu, C. K., Lisenfeld, U., Gao, Y., & Renaud, F. 2021, *ApJ*, **918**, 55
- Xu, C. K., Lu, N., Condon, J. J., Dopita, M., & Tuffs, R. J. 2003, *ApJ*, **595**, 665
- Yttergren, M., Misquitta, P., Sánchez-Monge, Á., et al. 2021, *A&A*, **656**, A83
- Yun, M. S., Verdes-Montenegro, L., del Olmo, A., & Perea, J. 1997, *ApJL*, **475**, L21
- Zwicky, F., & Kowal, C. T. 1968, *Catalogue of Galaxies and of Clusters of Galaxies*, Vol. 6 (Pasadena, CA: California Institute of Technology)